energy&fuels

pubs.acs.org/EF Article

Evolution of Shale Permeability under the Influence of Gas Diffusion from the Fracture Wall into the Matrix

Jie Zeng, Jishan Liu,* Wai Li, Yee-Kwong Leong, Derek Elsworth, and Jianchun Guo

Cite This: *Energy Fuels* 2020, 34, 4393−4406 Read Online

ACCESS | Metrics & More | Article Recommendations

ABSTRACT: Permeability is the most important property that controls the transfer of gas mass across a hierarchy of scales within a shale gas reservoir. When gas diffuses from the fracture wall into the matrix, the gas adsorbs onto shale grains. This adsorption may result in matrix swelling. In previous studies, it is commonly assumed that this swelling is uniform within the matrix. Under this assumption, the impact of the gas diffusion process would be neglectable. In this study, we hypothesize that this uniform swelling assumption is responsible for the inconsistencies between poroelastic solutions and experimental or field observations as reported in the literature. We introduce a volumetric ratio of the gas-invaded volume to the whole matrix volume to quantify the impact of matrix swelling volume expansion on the evolution of shale permeability. The gradual matrix pressure increase in the vicinity of fracture walls leads to local swelling. As the gas invaded zone expands within the matrix, the local effect weakens. When the matrix is completely invaded by the injected gas, a new homogeneous state is achieved, and the local effect ends. We find that the evolution of shale permeability from initial to final homogeneous states is a result of the propagation of the gas invaded area. We apply this approach to generate a series of shale permeability maps. These maps explain experimental observations under a spectrum of conditions from constant confining pressure, to constant average pore pressure, to constant effective stress, and to constant total volume conditions.

1. INTRODUCTION

Shale permeability is an elusive but fundamental parameter for shale gas formation characterization[1] and exploitation. Accurate characterization of permeability evolution during gas extraction or injection is crucial for gas migration modeling and productivity evaluation. This issue has been investigated both theoretically and experimentally.

1.1. State-of-the-Art Review of Theoretical Studies. Early in 1856, Darcy[2] proposed the basic equation for the fluid flow in porous media, known as Darcy's law. The Darcy permeability for the water flow through sand is simply a constant. Later, Klinkenberg[3] corrected the liquid permeability to describe the gas flow and stated that permeability is not only a property of the porous medium. It is also affected by the nature of the gas. Under an infinite pressure level, the permeability is a characteristic of the medium only. Based on Klinkenberg's theory, permeability can be defined as a function of pore pressure. To investigate the influence of applied stresses (overburden pressure), Somerton et al.[4] defined coal permeability as a function of the applied stress and permeability at zero stress. Their equation was treated as a good representation of the applied stress effects for both hydrostatic and triaxial tests. Rock permeability drops with increasing confining pressure or decreasing pore pressure.[5] The effective stress concept, which is originally defined as the difference between the confining stress and pore pressure, is extensively used to address permeability variation. Zoback and Byerlee[6] established an empirical linear equation which relates the permeability to confining pressure and pore pressure. Their results indicate that pore pressure plays a more significant role in determining permeability. Later on, Walsh[7] derived a nonlinear permeability expression where the influence of independent changes of pore pressure and confining pressure on permeability is finally depicted by the changes of effective stresses. Apart from that, more specific exponential relationships[8−11] and power law relationships[9,12] have been developed to handle the permeability evolution with effective stress variation. As for shale and coal formations, the impact of rock shrinkage/swelling caused by gas desorption/adsorption on permeability evolution needs to be included. Gray[13] incorporated shrinkage effects into coal effective stress estimation by using an equivalent sorption pressure concept, and rock shrinkage is directly related to the change of equivalent sorption pressure. Seidle et al.[14] extended the matchstick fractured reservoir geometry and derived a theoretical stress-permeability relation, considering desorption-induced shrinkage. The change of matrix spacing due to shrinkage is depicted by the product of a shrinkage coefficient and the pressure change. Their calculations indicate that the matrix shrinkage-induced permeability enhancement can offset the permeability drop caused by the stress increase. After that, Langmuir-type swelling/shrinkage strains were widely utilized in permeability models to handle rock swelling/shrinkage

Received: January 20, 2020
Revised: March 4, 2020
Published: March 5, 2020

https://dx.doi.org/10.1021/acs.energyfuels.0c00219
Energy Fuels 2020, 34, 4393−4406

effects.[10,11,15−17] To improve the accuracy in demonstrating swelling/shrinkage of rocks, the internal swelling/shrinkage stress and strain concepts were proposed and can account for the impact of matrix swelling on fracture aperture changes.[18−20] The localized effects come from partial matrix swelling/shrinkage and the variation of swelling/shrinkage at regional scales.[18,19] Based on the above models, permeability-pore-pressure curves and permeability-confining-pressure curves can be generated. However, these models commonly assumed that matrix-fracture fluid pressure equilibrium is achieved.[21] Under this pressure equilibrium assumption, the matrix swelling or shrinkage is uniform. Therefore, the swelling/shrinkage strain is uniform within the matrix. This assumption ignores the gradual gas diffusion or depletion processes which first occur at fracture (pore) surfaces and then propagate into the inner matrix. In this situation, the matrix swelling or shrinkage area expands from fracture surfaces to the inner matrix, resulting in nonuniform matrix swelling/shrinkage strains. Initially, when the matrix-fracture equilibrium state is broken by gas injection or depletion, matrix swelling or shrinkage is localized at the fracture surface and purely contributes to the reduction or increment of fracture (pore) aperture with almost no influence on the total rock volume. With the expansion of swelling/shrinkage areas, local effects gradually become marginal, and swelling/shrinkage of the whole rock affects permeability evolution. Then, when the matrix is fully invaded or depleted, uniform matrix swelling/shrinkage is achieved. Finally, when the pressure of fracture and matrix systems is stabilized, the final matrix-fracture equilibrium state is achieved. Actually, the final matrix-fracture equilibrium may never be achieved within a permeability-measurement time scale for shale and coal rocks.[22] The transition from localized deformation to global deformation between the initial and final equilibrium states triggers matrix-fracture interactions. To include matrix-fracture interactions, Zhang et al.[21] defined four overlapping systems which are connected by three cross-coupling relations. The numerical simulator explains matrix-fracture interactions under constant total volume and constant confining stress conditions. On the basis of Zhang et al.,[21] Ma et al.[23] added the influence of flow regimes on permeability evolution for gas injection, and Liu et al.[24] investigated matrix-fracture nonequilibrium through temporal and spatial evolution of effective stresses. These models are able to explain experimental results caused by matrix-fracture nonequilibrium for certain testing conditions. The magnitude of the matrix-fracture pressure difference represents the degree of the nonequilibrium state. However, the physical process of gas diffusion from fracture walls to matrices, which is one of the key processes for permeability evolution, was not explicitly included to describe matrix-fracture interactions, and the swelling/shrinkage strains are still assumed to be uniformly distributed within the matrix.

1.2. State-of-the-Art Review of Experimental Investigations. Apart from theoretical studies, experimental investigations were also extensively conducted to figure out the permeability evolution laws. After Darcy[2] proposed the constant permeability concept and Klinkenberg[3] corrected the gas permeability, Ferrell[25] noticed that the overburden pressure (reservoir confining pressure) can significantly reduce the permeability of deep and loosely consolidated reservoirs. This conclusion was obtained by using high-confining-pressure relative permeability tests, real injection data, combined relative permeability values and productivity increments, water-influx data, and pressure falloff tests.

Similar observations were found experimentally by Thomas and Ward.[26] When the overburden pressure reaches 20.68 MPa, the residual permeability of unfractured sandstone samples ranges from 14% to 37% of the original permeability. Wang and Park[27] conducted triaxial compression tests and found that the permeability drops with the increments in load. For shale rocks, the influence of flow regimes is strong.[17] Heller et al.[28] conducted experiments to examine the effective permeability of core samples from the Montney, Barnett, Marcellus, and Eagle Ford shale formations. Their data indicate that the slippage effects under low pressure conditions significantly increase the effective permeability. Yang et al.[29] performed pressure transient experiments on specimens from the Longmaxi shale formation to investigate the coupled effects of effective stresses and gas slippage on permeability. Their results show that the dominant factor that controls permeability shifts from gas slippage to effective stresses with the increase of pore pressure. Another essential influence on permeability evolution of sorbing porous media, such as shale and coal rocks, comes from sorption-induced volumetric strains.[30] Jin et al.[31] measured shale permeability by using different gas types and reported that the nitrogen permeability is higher than the argon permeability due to their different adsorption potentials. Argon's sorption potential is larger than that of nitrogen. Specifically, for permeability measurements under constant confining pressure conditions with increasing fracture (pore) pressure, Wei et al.[30] pointed out that permeability-pore-pressure relationships are normally classified into two types: the monotonous-increase type[32] and the v-shaped type.[33] Definitely, v-shaped permeability curves contradict the classical poroelasticity theory. The discrepancy between experimental results and theoretical calculations may come from matrix-fracture interactions. Wei et al.[30] evaluated the time-dependent coal permeability and observed a permeability transition from the initial reduction (local matrix swelling) to the later rebound (global swelling). Shi et al.[22] compared coal permeability measurement data from constant confining pressure and constant effective stress conditions. They concluded that the permeability behavior falls in the region between free-swelling and constant-total-volume solutions as a result of matrix-fracture (pore) interactions. Combining these experimental studies, one can find that shale permeability is determined by effective stresses, flow regimes, sorption-induced strains, and matrix-fracture (pore) nonequilibrium periods.

From the above literature review, we find that the long-term shale permeability prediction under the influence of the matrix-fracture (pore) nonequilibrium state is still challenging. This research aims at explaining permeability evolution based on the nonuniform swelling/shrinkage strain assumption which is realized by using the gas invaded/depleted matrix volume ratio. It is defined as the ratio of the gas invaded/depleted matrix volume to the total matrix volume and changes from zero to one with gas invaded/depleted volume expansion due to gas injection/extraction. The dynamic invaded/depleted volume ratio and uninvaded/undepleted volume ratio describe the magnitudes of global and local deformation caused by matrix swelling/shrinkage. Initially, the invade/depleted volume ratio is close to zero, global swelling/shrinkage is marginal, while local effects are significant. When it approaches the fully invaded/depleted state, the invade/depleted volume ratio is almost one. At that time, local effects disappear, while global ones reach their maximum contribution. Based on the nonuniform matrix swelling/shrinkage assumption, the range of permeability

https://dx.doi.org/10.1021/acs.energyfuels.0c00219
Energy Fuels 2020, 34, 4393−4406

between the initial and final equilibrium states can be obtained. The full spectrum of permeability ranges during a measurement procedure occupies an angle-shaped area in the permeability-pressure diagram, known as the permeability map. Permeability evolution for both gas injection and depletion can be consequently presented as maps instead of traditional permeability curves. The proposed model can deal with constant effective stress, constant average pore pressure, constant confining pressure, and constant total volume conditions.

2. CONCEPTUAL MODELS

In this section, conceptual models are introduced. Shale rocks consist of fracture-networks (primary gas flow channels) and matrix blocks. In this study, they are idealized as a matrix-block and fracture-network interwoven structure. Figure 1 shows the conceptual structure of the matrix-fracture (pore) system. Here, a is the spacing of flow channels (m), and b is the corresponding aperture (m). The flow channel can be nanopores or larger-scale fractures. The initial flow channel aperture is selected by matching with the initial permeability. The cross-sectional area, as shown in Figure 2, is rectangular. SEM images of shale samples show circular-, angular-, and slit-type pores.[34,35] By applying aspect ratios, this model can simulate different pore shapes through appropriate rectangular-shape approximations (Figure 2). Before gas injection or extraction, the system is under an equilibrium state. During gas injection, fracture (pore) pressure increases, and the gas adsorbed at fracture (pore) surfaces moves to the inner matrix by means of diffusion. This process first induces the swelling of matrix surfaces, which purely reduces fracture (pore) aperture without changing the bulk volume and refers to internal (local) swelling.[20,36] Meanwhile, the decreasing effective stress results in permeability enhancement. Therefore, during this period, the initial equilibrium no longer exists, and the permeability is determined by the net influence of effective stresses and the local swelling induced fracture aperture reduction. Then, as the invaded matrix volume propagates and occupies more matrix volumes, matrix swelling becomes more uniform. The swelling strain within the matrix also turns more uniform. This would increase the whole rock volume (matrix and fracture volumes), which enhances permeability. Local phenomena gradually become marginal due to more uniform swelling, approaching a new equilibrium state. Finally, matrices are fully infiltrated by injected gas, achieving uniform global swelling without any local effects.[20] Therefore, swelling effects, which follow the Langmuir-adsorption law,[10] shift from local phenomena to global ones. Figure 3(a) shows the evolution of matrix, fracture, and bulk volumes from the initial state to the fully invaded state. As for gas depletion, the gas is released from matrices due to the fracture

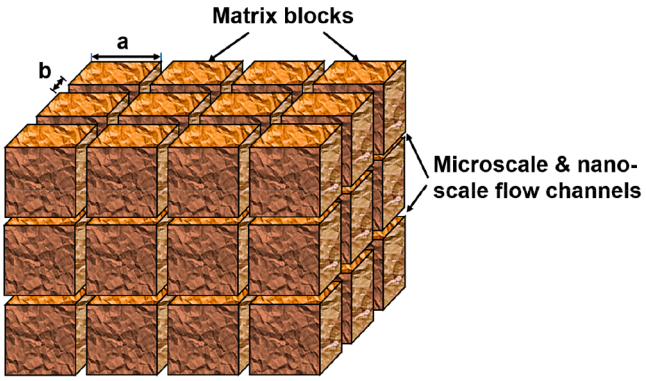

Figure 1. Schematic of idealized shale rocks composed of cubic matrix elements and micro- and nanochannels (after Pan et al.[37] and van Golf-Racht[38]).

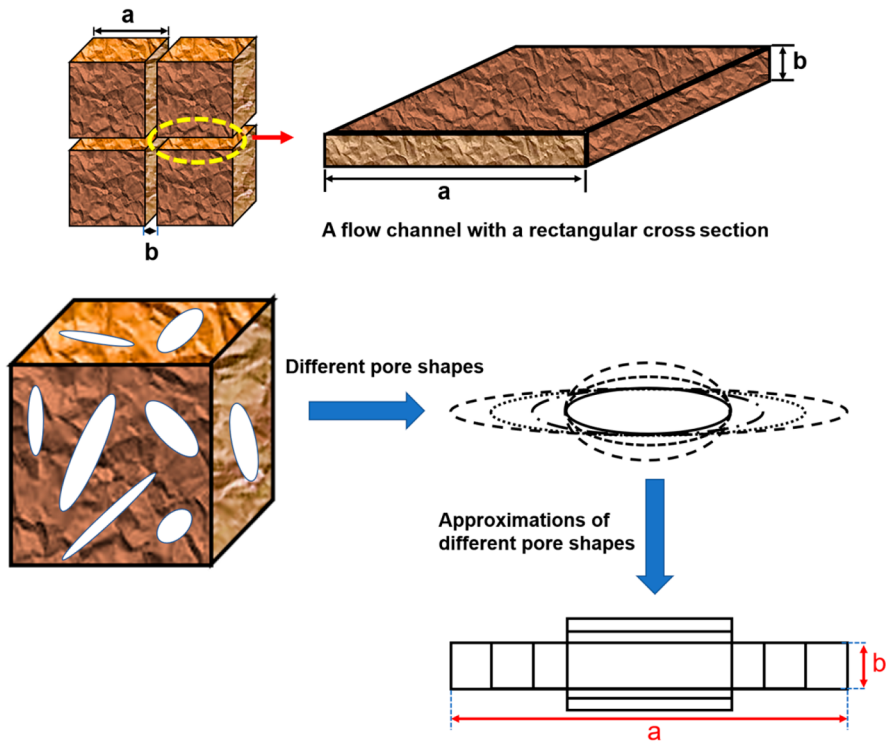

Figure 2. Schematic of approximations of different pore shapes in shale rocks.

https://dx.doi.org/10.1021/acs.energyfuels.0c00219
Energy Fuels 2020, 34, 4393−4406

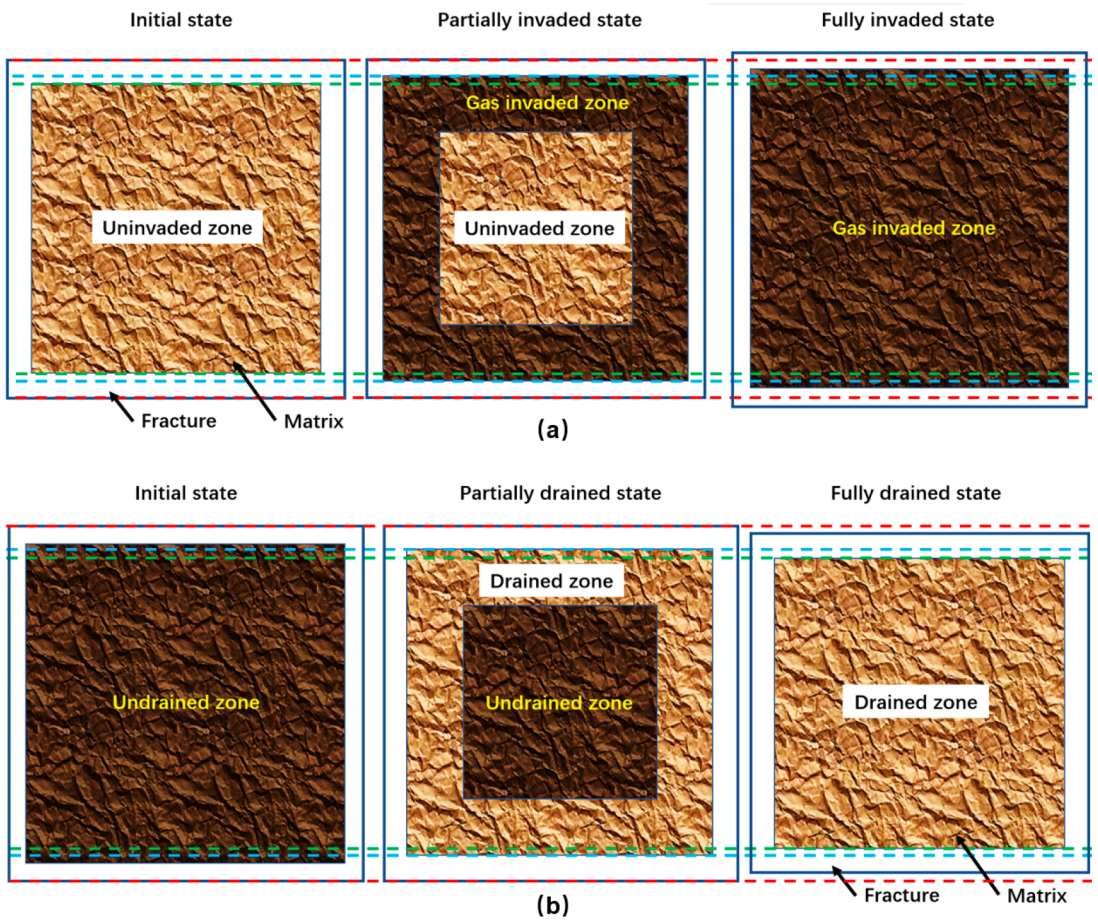

Figure 3. Schematic of local and global swelling/shrinkage's contribution to the matrix and fracture (pore) volume change: (a) gas injection and (b) gas depletion (after Peng et al.[20]).

(pore) pressure decline, resulting in matrix shrinkage. Initially, shrinkage occurs at matrix surfaces and purely enlarges the aperture of flow channels. Therefore, local matrix shrinkage enhances shale permeability, and the effective stress increment would reduce the permeability. Once again, the permeability at this stage is controlled by the net effect of effective stresses and local shrinkage, and the shrinking zones within matrices would propagate from fracture (pore) walls to the inner matrix. As drained zones continuously expand, matrix shrinkage becomes more uniform, and the shrinkage of the whole rock gradually becomes noticeable. Similar to swelling, shrinkage effects also shift from local shrinkage to global shrinkage. Finally, the whole matrix becomes drained, resulting in uniform global shrinkage and the disappearance of local shrinking. Figure 3(b) shows the evolution of matrix, fracture, and bulk volumes from the initial state to the fully drained state. The evolution of gas invaded and drained zones is depicted by Figure 4. Here, L_m is the side-length of matrix blocks (m), L_{m0} is the initial side-length of matrix blocks (m), L_s is the invaded/drained zone thickness (m), and $L_m \approx Lm_0 \approx a$. The dynamic invaded/drained matrix volume ratios are selected to quantify local/global sorption-induced strain changes and change from zero to one during gas injection/extraction. Therefore, the contribution of local swelling gradually drops to zero, while the contribution of global swelling continuously increases to the maximum level, which depicts the transition from local swelling/shrinkage to global swelling/shrinkage.

3. FORMULATION OF CONCEPTUAL MODELS

With the above-mentioned considerations and understanding, we can formulate these conceptual models based on the poroelasticity theory. According to Figure 1, the intrinsic permeability of a flow channel is[39]

$$k_{int} = \frac{b^2}{12} \tag{1}$$

Then, the porosity and bulk permeability can be expressed as[39]

$$\phi = \frac{ba^2}{a^3} + \frac{ba^2}{a^3} + \frac{ba^2}{a^3} = \frac{3b}{a} \tag{2}$$

$$k = k_{int}\left(\frac{ba}{a^2} + \frac{ba}{a^2}\right) = \frac{b^3}{6a} = \frac{a^2\phi^3}{162} \tag{3}$$

Here, ϕ is the effective porosity defined by fracture spacing and aperture for the bulk gas flow. Therefore, the bulk permeability ratio is written as[37]

$$\frac{k}{k_0} = \left(\frac{a^2}{a_0^2}\right)\left(\frac{\phi^3}{\phi_0^3}\right) \tag{4}$$

where the subscript 0 represents initial-time properties. To include the influence of flow regimes, the apparent permeability is defined as follows based on the correction coefficient for variable flow regimes[40,41]

https://dx.doi.org/10.1021/acs.energyfuels.0c00219
Energy Fuels 2020, 34, 4393−4406

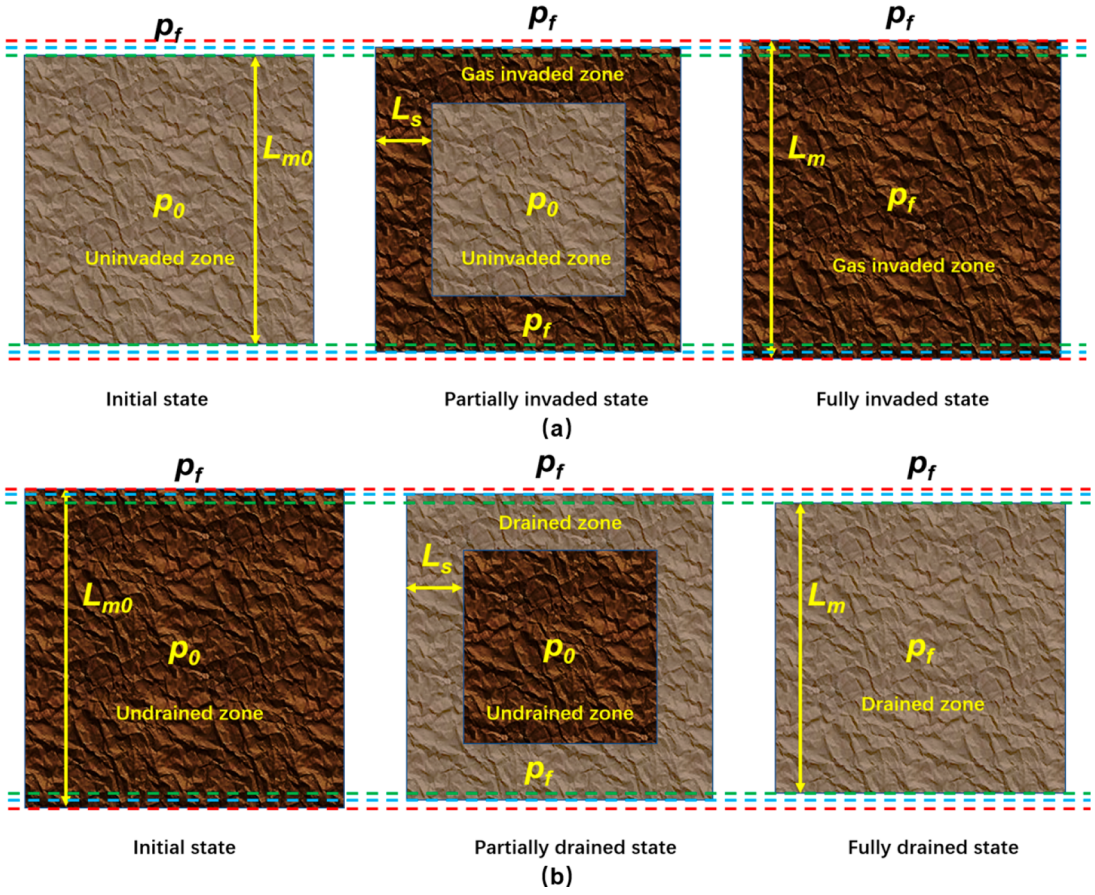

Figure 4. Evolution of gas invaded and drained zones: (a) gas injection and (b) gas depletion (after Peng et al.[20]).

$$k_{app} = kC(\beta_a)(1 + \alpha_k Kn)\left(1 + \frac{6Kn}{1 - b_k Kn}\right) = \frac{a^2\phi^3}{162}C(\beta_a)(1 + \alpha_k Kn)\left(1 + \frac{6Kn}{1 - b_k Kn}\right) \quad (5)$$

where β_a is the aspect ratio which equals a/b (width/height), Kn is the Knudsen number, a_k is a coefficient which is a function of Kn, $C(\beta_a)$ is the correction factor for different flow channel shapes, and $b_k = -1$. Here, the Knudsen number is defined as $Kn = \lambda/b$, where λ is the molecular mean free path (m). The mean free path is given by[17,42]

$$\lambda = \frac{K_B T}{\sqrt{2}\,\pi\delta^2 p} \quad (6)$$

where K_B is the Boltzmann constant (1.3806×10^{-23}J/K), T is the temperature (K), and δ is the diameter of gas molecules (m).[43] The coefficients a_k and $C(\beta_a)$ are expressed as[44,45]

$$\alpha_k = \alpha_{ki}\frac{2}{\pi}\tan^{-1}(\alpha_1 Kn^{\beta_2}) \quad (7a)$$

$$C(\beta_a) = 1 - \frac{192}{\beta_a\pi^5}\sum_{i=1,3,5,\ldots}^{\infty}\frac{\tanh[i\pi\beta_a/2]}{i^5} \quad (7b)$$

where a_{ki} represents a constant asymptotic value in the free molecular regime ($64/(15\pi)$), $\alpha_1 = 4$, and $\beta_2 = 0.4$. Eq 7b is the same as Wu et al.[44] but is a little different from White and Corfield.[45] This is because only by using eq 7b can we obtain correction factors 42.17%, 68.60%, and 84.24% with aspect ratios 1, 2, and 4, respectively, as mentioned and verified by Karniadakis et al.[41] Consequently, the apparent permeability ratio is

$$\frac{k_{app}}{k_{app0}} = \frac{a^2\phi^3 C(\beta_a)(1 + \alpha_k Kn)\left(1 + \frac{6Kn}{1 - b_k Kn}\right)}{a_0^2\phi_0^3 C(\beta_{a0})(1 + \alpha_{k0}Kn_0)\left(1 + \frac{6Kn_0}{1 - b_k Kn_0}\right)} \quad (8)$$

In order to use eq 8 for permeability evolution analyses, $\frac{a}{a_0}$ and $\frac{\phi}{\phi_0}$ need to be figured out, and the variation of $C(\beta_a)$ and Kn should also be calculated as a function of pressure and flow channel aperture. According to Cui and Bustin[10] and Cao et al.,[46] we have

$$\frac{dV_b}{V_b} = -\frac{d\bar{\sigma}}{K} + \frac{\alpha dp}{K} + d\varepsilon_{bs} \quad (9)$$

where V_b is the bulk volume (m^3), K is the bulk modulus (Pa), $\bar{\sigma}$ is the mean normal stress or confining pressure (Pa), α is the Biot coefficient ($\alpha = 1 - K/K_s$),[10] K_s is the matrix rock modulus (Pa), p is the fracture (pore) pressure (Pa), and ε_{bs} is the sorption-induced bulk volumetric strain. Assuming that K and α are constant and integrating eq 9 yield

$$\frac{V_b}{V_{b0}} = \exp\left[-\frac{1}{K}(\bar{\sigma} - \bar{\sigma}_0) + \frac{\alpha}{K}(p - p_0) + (\varepsilon_{bs} - \varepsilon_{bs0})\right] = \frac{a^3}{a_0^3} \quad (10)$$

Therefore,

https://dx.doi.org/10.1021/acs.energyfuels.0c00219
Energy Fuels 2020, 34, 4393−4406

$$\frac{a}{a_0} = \sqrt[3]{\frac{V_b}{V_{b0}}} = \exp\left[-\frac{1}{3K}(\bar{\sigma} - \bar{\sigma}_0) + \frac{\alpha}{3K}(p - p_0) + \frac{1}{3}(\varepsilon_{bs} - \varepsilon_{bs0})\right] \tag{11}$$

Similarly, the following equation can be written to denote the fracture (pore) volume change, considering local effects[19]

$$\frac{dV_f}{V_f} = -\frac{d\bar{\sigma}}{K_f} + \frac{\gamma dp}{K_f} + d\varepsilon_{bs} + d\varepsilon_{lfs} \tag{12}$$

where V_f is the fracture (pore) volume (m^3), K_f is the modulus of the fracture (pore) volume (Pa), ε_{lfs} is the sorption-induced internal fracture (pore) volumetric strain, and $\gamma = 1 - K_f/K_s$. Here, ε_{lfs} is a negative if the local strain reduces the fracture (pore) volume. Based on eqs 9 and 12, the following relationship can be obtained[10,19]

$$\frac{d\phi}{\phi} = \frac{dV_f}{V_f} - \frac{dV_b}{V_b} = \left(\frac{1}{K} - \frac{1}{K_f}\right)(d\bar{\sigma} - dp) + d\varepsilon_{lfs} \tag{13}$$

Integrating the above equations yields

$$\frac{\phi}{\phi_0} = \exp\left\{\left(\frac{1}{K} - \frac{1}{K_f}\right)[(\bar{\sigma} - \bar{\sigma}_0) - (p - p_0)] + (\varepsilon_{lfs} - \varepsilon_{lfs0})\right\} \tag{14}$$

Recalling eq 2, we have

$$\frac{b}{b_0} = \frac{\phi}{\phi_0}\frac{a}{a_0} = \exp\left\{\left(\frac{1}{K} - \frac{1}{K_f}\right)[(\bar{\sigma} - \bar{\sigma}_0) - (p - p_0)] + (\varepsilon_{lfs} - \varepsilon_{lfs0})\right\} \times \exp\left[-\frac{1}{3K}(\bar{\sigma} - \bar{\sigma}_0) + \frac{\alpha}{3K}(p - p_0) + \frac{1}{3}(\varepsilon_{bs} - \varepsilon_{bs0})\right] \tag{15}$$

$$\frac{\beta_a}{\beta_{a0}} = \frac{\phi_0}{\phi} = \exp\left\{-\left(\frac{1}{K} - \frac{1}{K_f}\right)[(\bar{\sigma} - \bar{\sigma}_0) - (p - p_0)] - (\varepsilon_{lfs} - \varepsilon_{lfs0})\right\} \tag{16}$$

Therefore, we obtain

$$b = b_0 \exp\left[\left(\frac{2}{3K} - \frac{1}{K_f}\right)(\bar{\sigma} - \bar{\sigma}_0) - \left(\frac{2}{3K} + \frac{1}{3K_s} - \frac{1}{K_f}\right)(p - p_0) + \frac{1}{3}(\varepsilon_{bs} - \varepsilon_{bs0}) + (\varepsilon_{lfs} - \varepsilon_{lfs0})\right] \tag{17}$$

$$\beta_a = \beta_{a0} \exp\left\{-\left(\frac{1}{K} - \frac{1}{K_f}\right)[(\bar{\sigma} - \bar{\sigma}_0) - (p - p_0)] - (\varepsilon_{lfs} - \varepsilon_{lfs0})\right\} \tag{18}$$

To simulate the temporal and spatial evolution of local strains, we employ a volume ratio concept. According to the definition of volumetric strains, the sorption/desorption-induced local matrix volume change can be expressed by[19]

$$\Delta V_{lms} = \varepsilon_{lms} V_{mor} \tag{19}$$

where ε_{lms} is the internal (local) matrix strain, and V_{mor} is the reference original matrix volume (m^3). Local matrix swelling reduces the fracture (pore) volume and the volume reduction is equal to the local matrix volume increment ($\Delta V_{lms} = -\Delta V_{lfs}$). In this study, ε_{lms} is the matrix total volume averaged strain, and there is no need to further multiply it by an invaded volume ratio. Therefore, the relationship between the local matrix strain and local fracture (pore) strain can be written as[19]

$$\varepsilon_{lfs} = \frac{\Delta V_{lfs}}{V_{for}} = -\frac{\Delta V_{lms}}{V_{for}} = -\frac{\varepsilon_{lms} V_{mor}}{V_{for}} \approx -\frac{\varepsilon_{lms}(V_{mor} + V_{for})}{V_{for}} = -\frac{\varepsilon_{lms}}{\phi_{or}} \tag{20}$$

where V_{for} is the reference original fracture (pore) volume (m^3), and ϕ_{or} is the reference original porosity. Here, we use reference original properties to distinguish initial properties because we can assume that the initial strains are not zero. The local strain change causes local effects. The local matrix strain difference is a function of time and space. Recalling Figure 4, the dynamic invaded/drained zone thickness is given by

$$L_s = \sqrt{\eta_m t} \tag{21}$$

where η_m is the pressure-dependent pseudodiffusivity of matrix blocks (m^2/s), and t is time (s). Here $\eta_m/\eta_{m0} = \lambda/\lambda_0$[47] because the matrix grain pores are extremely small. We can use the mean free path to replace the matrix block pore radius when we define the diffusivity term.[47] The matrix block pseudodiffusivity is extremely low because it would take a long time for the invaded zone to equivalently reach fracture (pore) pressure. Here, matrix block pores are not effective flow channels for gas permeability measurements. The volume ratio of invaded/drained zones to matrix blocks can be expressed by ($L_m \approx L_{m0} \approx a$)

$$r_{inv} = \frac{L_{m0}^3 - (L_{m0} - 2L_s)^3}{L_{m0}^3} (L_{m0} - 2L_s \geq 0) \tag{22}$$

If $L_{m0} - 2L_s < 0$, $r_{inv} = 1$. This means the matrix block is fully invaded by the injected gas. As mentioned before, with the invaded/drained volume increases, global swelling/shrinkage effects become more noticeable. In contrast, when the swelling/shrinkage volume expands from matrix surfaces to the whole matrix block, local effects gradually disappear. The uninvaded/undrained zone and invaded/drained zone volume ratios represent the magnitudes of local and global effects, respectively. Therefore, local fracture strain and global strain changes can be written as

$$\varepsilon_{lfs} - \varepsilon_{lfs0} = -\frac{\varepsilon_{lms} - \varepsilon_{lms0}}{\phi_{or}} = -\frac{\varepsilon_{Lm}}{\phi_{or}}\left(\frac{p}{p + p_{Lm}} - \frac{p_0}{p_0 + p_{Lm}}\right)(1 - r_{inv}), \quad \text{for } 0 \leq t \leq \frac{L_{m0}^2}{4\eta_m} \tag{23a}$$

$$\varepsilon_{lfs} - \varepsilon_{lfs0} = 0, \quad \text{for } t > \frac{L_{m0}^2}{4\eta_m} \text{ and } r_{inv} = 1 \tag{23b}$$

$$\varepsilon_{bs} - \varepsilon_{bs0} = \varepsilon_{Lb}\left(\frac{p}{p + p_{Lb}} - \frac{p_0}{p_0 + p_{Lb}}\right) r_{inv}, \quad \text{for } 0 \leq t \leq \frac{L_{m0}^2}{4\eta_m} \tag{24a}$$

$$\varepsilon_{bs} - \varepsilon_{bs0} = \varepsilon_{Lb}\left(\frac{p}{p + p_{Lb}} - \frac{p_0}{p_0 + p_{Lb}}\right), \quad \text{for } t > \frac{L_{m0}^2}{4\eta_m} \text{ and } r_{inv} = 1 \tag{24b}$$

where ε_{Lm} is the Langmuir strain constant of matrices,[19] p_{Lm} is the matrix Langmuir pressure constant (Pa), ε_{Lb} is the Langmuir strain constant of the shale bulk, and p_{Lb} is the bulk Langmuir pressure constant (Pa). In eqs 23 and 24, both r_{inv} and fracture (pore) pressure p determine the evolution of local and global effects, and p can be either a constant or a time-dependent variable because it may take a certain time for fractures (pores) to reach a uniform-pressure level. Only in constant average fracture (pore) cases, p is a constant. Combining eqs 6–8, 11,

https://dx.doi.org/10.1021/acs.energyfuels.0c00219
Energy Fuels 2020, 34, 4393−4406

14, 17, 18, and 21− 24, the permeability ratio for gas injection can be expressed as

$$\frac{k_{app}}{k_{app0}} = \exp\left\{\left(\frac{7}{3K} - \frac{3}{K_f}\right)(\bar{\sigma} - \bar{\sigma}_0) - \left(\frac{7}{3K} - \frac{3}{K_f} + \frac{2}{3K_s}\right)(p - p_0) + \frac{2\varepsilon_{Lb}}{3}\left(\frac{p}{p + p_{Lb}} - \frac{p_0}{p_0 + p_{Lb}}\right)\left[\frac{L_{m0}^3 - (L_{m0} - 2L_s)^3}{L_{m0}^3}\right] - \frac{3\varepsilon_{Lm}}{\phi_{or}}\left(\frac{p}{p + p_{Lm}} - \frac{p_0}{p_0 + p_{Lm}}\right)\left[1 - \frac{L_{m0}^3 - (L_{m0} - 2L_s)^3}{L_{m0}^3}\right]\right\} \times \frac{C(\beta_a)(1 + \alpha_k Kn)\left(1 + \frac{6Kn}{1 - b_k Kn}\right)}{C(\beta_{a0})(1 + \alpha_{k0} Kn_0)\left(1 + \frac{6Kn_0}{1 - b_k Kn_0}\right)}, \quad \text{for } 0 \le t \le \frac{L_{m0}^2}{4\eta_m} \tag{25a}$$

$$\frac{k_{app}}{k_{app0}} = \exp\left[\left(\frac{7}{3K} - \frac{3}{K_f}\right)(\bar{\sigma} - \bar{\sigma}_0) - \left(\frac{7}{3K} - \frac{3}{K_f} + \frac{2}{3K_s}\right)(p - p_0) + \frac{2\varepsilon_{Lb}}{3}\left(\frac{p}{p + p_{Lb}} - \frac{p_0}{p_0 + p_{Lb}}\right)\right] \frac{C(\beta_a)(1 + \alpha_k Kn)\left(1 + \frac{6Kn}{1 - b_k Kn}\right)}{C(\beta_{a0})(1 + \alpha_{k0} Kn_0)\left(1 + \frac{6Kn_0}{1 - b_k Kn_0}\right)}, \quad \text{for } t > \frac{L_{m0}^2}{4\eta_m} \tag{25b}$$

where the fracture (pore) pressure for gas injection is given by[48−50]

$$p = p_0 + (p_e - p_0)\left[1 - \exp\left(-\frac{t}{t_d}\right)\right] \tag{26}$$

Here, p_e is the final equilibrium pressure of fractures (pores), namely, the injection pressure (Pa), and t_d is the characteristic time (s) which can be determined by the pressure difference between p_e and p_0.[48,50] The beauty of this model is that eqs 25 and 26 are also capable for gas depletion cases. $t_d = (p_e - p_0)/C$ and $t_d = -(p_e - p_0)/C$ are for gas injection and depletion, respectively. Here, C is a constant coefficient (Pa/s).[50] Therefore, the proposed model is a general permeability model for both gas injection and depletion. In this model, K and K_f are calculated as follows[10]

$$K = E/[3(1 - 2\nu)] \tag{27}$$

$$K_f = \phi_{or} K/\alpha \tag{28}$$

where E is the Young's modulus (Pa) and ν is Poisson's ratio.

4. MODEL VERIFICATION

In this section, the proposed model is verified against shale permeability measurement data. In the literature, most laboratory results are obtained from constant effective stress conditions, constant confining pressure conditions, and constant average pore pressure conditions,[36] and our calculations are validated against experimental data from the three types of permeability measurement conditions.

4.1. Constant Terzaghi Effective Stress Conditions. Case 1 analyzed shale permeability at different fracture (pore) pressure and confining pressure, while the Terzaghi effective stress $(\bar{\sigma} - p)$ is a constant with $\Delta\bar{\sigma} = \Delta p$.[43] The shale sample was collected from the Montney formation in Canada. Permeability was measured at room temperature (25 °C), and methane was used as the flowing fluid. During the test, the confining fluid generated isotropic stresses on the sample with a fixed mean effective stress $(\bar{\sigma} - p)$ at 10 MPa. In our simulation, the fracture (pore) aperture and spacing are selected to satisfy the initial bulk apparent permeability (2×10^{-18} m^2). The original porosity we use can be equal to the measured porosity or smaller. This is because the original porosity for gas transport only accounts for the fracture contributed porosity according to our conceptual model. Besides, the porosity measurement condition is different from the permeability testing condition. Other input parameters, as shown in Figure 5(a), are all selected from the original paper and related studies.[36,43,51] The mechanical properties of this case and the following cases are determined by experimental data matching and are in accordance with the ranges of properties provided in the literature.[52−56] According to the classical poroelasticity theory, the permeability should be a constant under the constant Terzaghi effective stress condition[10]

$$\frac{k}{k_0} = \left(\frac{\phi}{\phi_0}\right)^3 = \exp\left\{3\left(\frac{1}{K} - \frac{1}{K_f}\right)[(\bar{\sigma} - \bar{\sigma}_0) - (p - p_0)]\right\} = 1 \tag{29}$$

Definitely, the constant permeability conclusion obtained from eq 29 cannot explain the experimental observations. Figure 5(a) presents permeability evolution at different times and fracture (pore) pressure (injection pressure) levels. It can be seen that even if the effective stress is constant, the permeability ratio still changes with time. Due to local effects, fracture aperture is reduced, generating a significant bulk permeability decline. The higher the fracture (pore) pressure is, the lower the permeability would be during this period. This is because a higher-pressure level results in a stronger local sorption-induced strain. Later, the expansion of invaded zones makes matrix swelling more uniform, which weakens local effects and recovers bulk permeability. Finally, the permeability reaches a constant value when matrix and fracture systems achieve a new equilibrium state. By comparing Figures 5(a) and 5(b), one can find that the increments in fracture (pore) pressure generate apparent permeability reductions if flow regime effects are included. The flow regime is defined based on the Knudsen number.[57] The Knudsen number calculated ranges from 0.098 to 0.049 in this case, which indicates that the flow regime falls in the slip flow regime ($0.01 < Kn < 0.1$). The reason for the permeability loss under the final stable state is that higher-pressure conditions mitigate the slippage effects within micro- and nanoscale flow channels. If flow regime's influence is ignored, the final stable permeability is close to the initial one as effective stresses are constant, as shown in Figure 5(b). The slight increment of the stable permeability is caused by global swelling. These permeability curves can be transformed into vertical bars which represent the range of the permeability ratio under a certain injection pressure level. Therefore, the permeability evolution can be presented as a map instead of using a curve. Figure 5(c) shows the permeability map for measured permeability curve matching. Theoretically, the final stable permeability should be lower than the initial one if the fracture aperture is extremely small due to gas slippage weakening. However, most measured permeability values are much smaller than the calculated stable permeability. This indicates that the permeability values were collected under the intermediate nonequilibrium states. We can also draw two boundaries that envelope all calculated results. The upper boundary represents the unit permeability ratio at the initial time. The lower boundary depicts permeability ratios measured with maximum

https://dx.doi.org/10.1021/acs.energyfuels.0c00219
Energy Fuels 2020, 34, 4393−4406

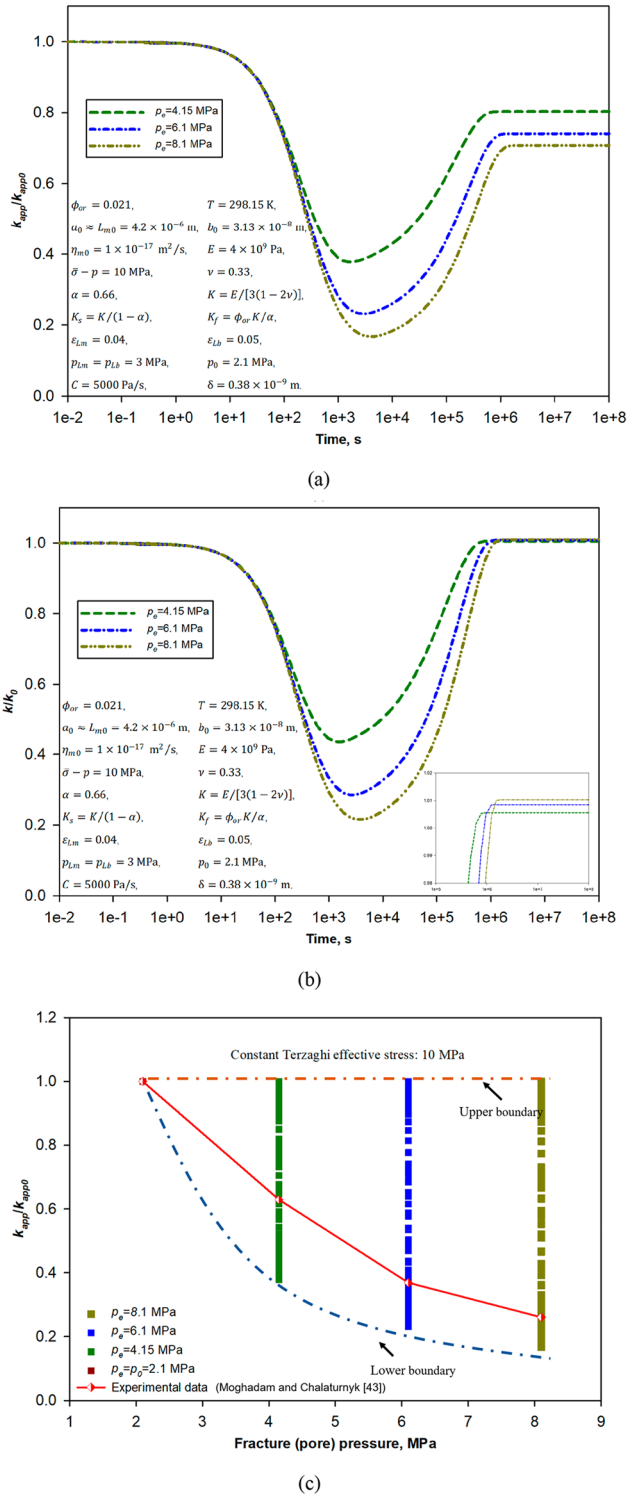

Figure 5. Evolution of shale permeability under a constant Terzaghi effective stress condition: (a) simulation results of permeability ratios; (b) simulation results of permeability ratios without flow regime's influence; and (c) comparison of experimental data and simulation results.

local strain impacts, and the lower boundary is dominated by local swelling.

4.2. Constant Confining Pressure Conditions. For constant confining pressure cases, we analyze the data from two experiments (case 2 and case 3) which show different permeability evolution laws. The input parameters for simulation of the two cases are all selected from the original papers and related studies.[36,58−60] Case 2 was run under the same confining and axial stresses (7 MPa), and room temperature with the fracture (pore) pressure (injection pressure) increased from 1.1 to 5.05 MPa.[58] In this experiment, CO_2 was injected as the flowing fluid. The initial apparent permeability is 3.03×10^{-19} m^2. Similar to case 1, the evolution of permeability shows a v-shaped curve though it is more asymmetric, as shown in Figure 6(a), and a higher fracture

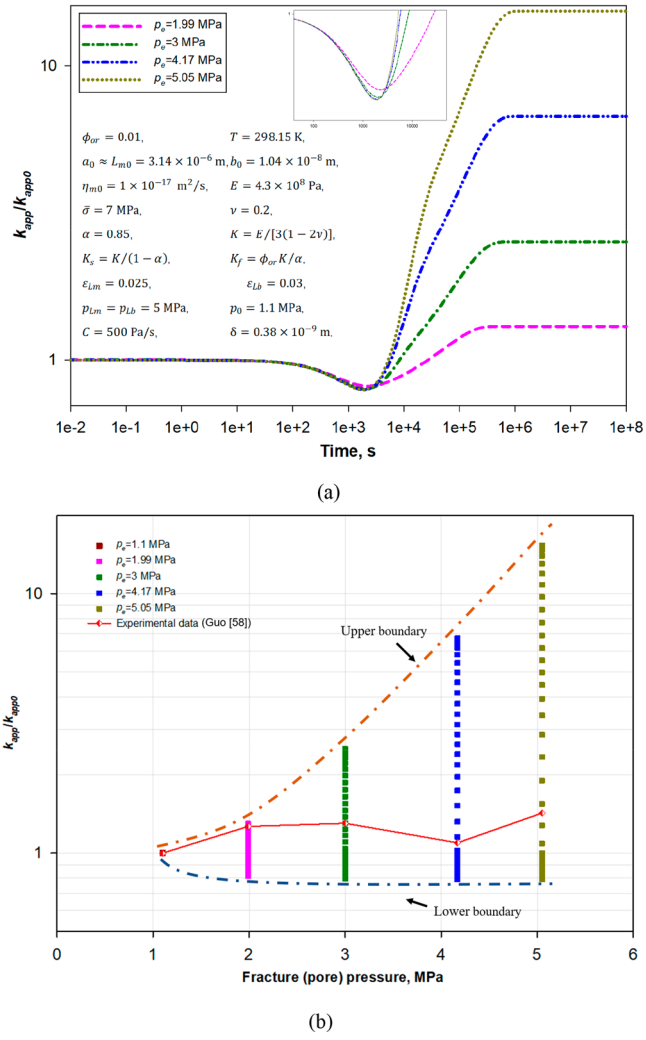

Figure 6. Evolution of shale permeability under a constant confining pressure condition (case 2): (a) simulation results and (b) comparison of experimental data and simulation results.

(pore) pressure also induces a heavier local swelling strain. However, the impact of local strains in this case is smaller possibly due to a lower rock adsorbability. The final stable permeability values are all larger than the initial permeability due to the reduction of effective stresses. As for experimental data (Figure 6(b)), the measured permeability values are higher than the initial one as well. In the first several stages, with fracture (pore) pressure increases, permeability increments can be observed, which is in accordance with our common knowledge. However, the permeability evolution does not follow a monotonical increasing law. A permeability drop under 4.17 MPa injection pressure was documented. Based on the classical

https://dx.doi.org/10.1021/acs.energyfuels.0c00219
Energy Fuels 2020, 34, 4393−4406

poroelasticity theory, one cannot explain the permeability drop during the fracture pressure (injection pressure) increasing procedure. It indicates that the measured values may not be the final stable permeability of the corresponding injection pressure levels, which gives a possible reason for the abnormal permeability ratio. The permeability map in Figure 6(b) is also bounded by two boundaries. The upper boundary is mainly controlled by effective stresses, while the lower one is dominated by sorption induced local strains. The experiment in case 3 was performed on a shale sample upon CO_2 injection at a constant confining stress (10 MPa).[59] The initial apparent permeability was collected at 3.9×10^{-15} m^2, which is higher than that in other cases due to the existence of the relatively large flow channel. In this situation, flow regime's influence is marginal compared with case 1. Theoretically, the stable permeability should be higher than the initial one, as indicated by Figure 7(a). However,

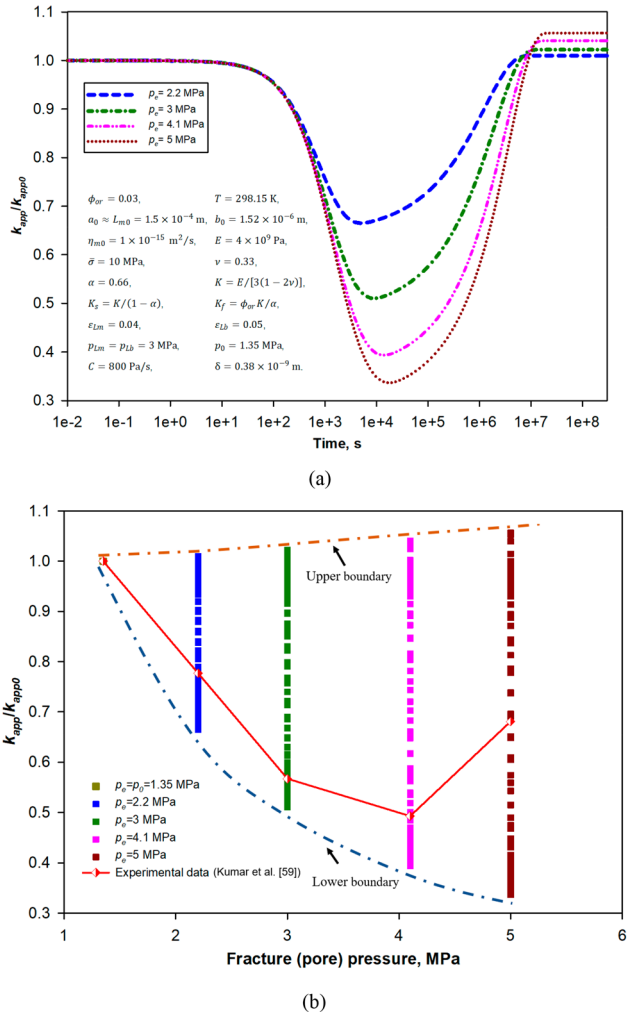

Figure 7. Evolution of shale permeability under a constant confining pressure condition (case 3): (a) simulation results and (b) comparison of experimental data and simulation results.

laboratory results in Figure 7(b) show that all measured values are lower than the initial permeability, and the curve exhibits a v-shaped evolution law. This discrepancy between the theoretical calculation and laboratory work can be explained by our permeability map in Figure 7(b). Once again, the permeability tends to be measured under nonequilibrium conditions. By comparing cases 2 and 3, one can also conclude that the distinct evolution behavior of the two cases could come from their different adsorption and mechanical properties.

4.3. Constant Average Pore Pressure Conditions. In terms of constant average fracture (pore) pressure experiments, the matrix-fracture systems within the samples are under an equilibrium state. Therefore, the dynamic transition between local and global swelling no longer exists. As a result, no permeability map can be generated. The experiment (case 4) we analyze was performed under a constant average fracture (pore) pressure condition (1.6 MPa) with identical axial and confining stresses.[61] The temperature of the system was kept at 45 °C (±1 °C). During the experiment, methane was injected as the injection fluid, and the confining pressure increased from 7.1 to 30 MPa. The initial permeability was measured at 2.3×10^{-17} m^2. Input parameters for our simulation are collected from the original paper and related research.[36,51,60,61] Figure 8 illustrates the comparison of experimental data and simulation results. An excellent agreement between testing results and our calculation has been achieved. The fracture aperture would become smaller with an increasing confining pressure level, which reduces the permeability, and the aperture reduction would also enhance gas slippage, which mitigates the permeability drop. Therefore, ignoring flow regime's impact can cause the underestimation of permeability during the confining pressure increasing process with the same input parameters. Errors becomes more noticeable when the pressure increment turns larger.

5. DISCUSSION OF POSSIBLE MODIFICATIONS

5.1. Permeability Curves and Maps for Gas Depletion. In fact, the proposed model is also capable for depicting gas depletion processes. In this model, the only difference between gas injection and extraction is that the initial pressure for gas extraction is higher than the final equilibrium pressure (the pressure of the next test). In this section, we first consider two experimental conditions including constant effective stress and constant confining pressure conditions and generate corresponding permeability maps. Then, the permeability evolution of a constant average fracture (pore) pressure case is also provided. For that case, we mainly focus on comparing the influence of flow regimes. Figures 9(a)–9(c) demonstrate permeability evolution of a constant Terzaghi effective stress case. The effective stress is maintained at 10 MPa, and the basic input parameters are the same as case 1. Different from gas injection, n-shaped permeability curves are obtained. In the first stage, permeability increases due to local matrix shrinkage. Then, a permeability decreasing stage occurs because local effects gradually disappear and are transformed into the shrinkage of the whole rock. Finally, permeability stabilization is achieved when the whole system reaches a new equilibrium state. The final stable permeability can be higher than the initial one due to gas slippage (Figure 9(a)), and gas slippage enhances the permeability. As for those without slip effects, the final permeability is determined by global shrinkage. As shown in Figure 9(b), a heavier pressure drop during gas depletion generates greater bulk shrinkage and lower permeability. The final permeability drop in Figure 9(b) is not significant due to the relatively small pressure change. Similarly, a permeability map is given in Figure 9(c) with lower and upper limits as well. Conversely, the upper limit defines the absorbability of the rock (local shrinkage level), while the lower limit is a horizontal line with a unit permeability ratio; and in no slip flow cases, the lower boundary depicts the magnitude of global shrinkage. Figures 10(a) and 10(b) present permeability curves and the

https://dx.doi.org/10.1021/acs.energyfuels.0c00219
Energy Fuels 2020, 34, 4393−4406

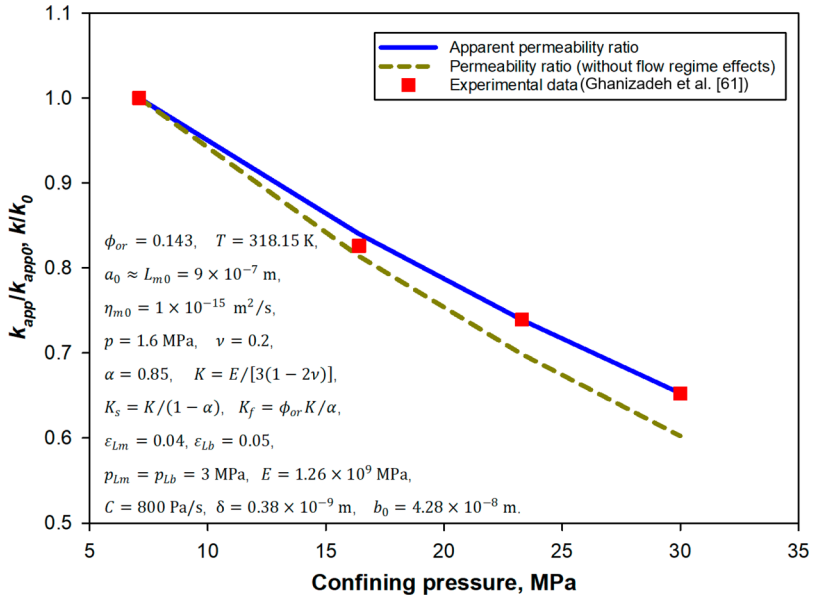

Figure 8. Comparison of experimental data and simulation results for a constant average fracture (pore) pressure case.

corresponding permeability map for a constant confining pressure case. The basic parameters are the same as case 3 with a fix confining pressure of 10 MPa. Under this test condition, permeability curves are also n-shaped. Because the fracture aperture of this case is sufficiently large, the flow regime's influence can be ignored, and the final stable permeability is determined by effective stresses and mechanical properties. In constant confining pressure cases, the global shrinkage's influence at late times can be easily masked by the impacts of effective stresses and flow regimes. Therefore, the upper and lower boundaries are determined by local shrinkage and effective stresses, respectively. Figure 11 shows a constant fracture (pore) pressure case with decreasing confining stresses. Since the matrix-fracture system is under an equilibrium pressure condition, the permeability evolution is simply dominated by effective stresses and flow regimes. With the confining pressure decreases, the fracture aperture becomes larger, which results in a permeability increment. However, larger aperture also mitigates gas slippage. Thus, with the same input data, the calculated results from no slip cases would overestimate the bulk permeability ratio. Errors increase when the pressure drop becomes larger.

5.2. Modified Equations for Constant Total Volume Conditions during Gas Injection. The above investigations are all for stress-controlled conditions. Another situation this model can deal with is gas injection under constant total volume conditions. The fracture spacing is a constant, so we have $a/a_0 = 1$. Gas depletion is not considered here because one cannot achieve a constant total bulk volume during gas extraction. According to Peng et al.,[19] a monotone decline of permeability can be observed during gas injection because the adsorption-induced matrix strains completely contribute to the reduction of fracture (pore) aperture without bulk rock swelling. When the total sample volume is fixed, global swelling strains and the bulk volume change are zero. Therefore, eq 10 becomes

$$\frac{V_b}{V_{b0}} = \exp\left[-\frac{1}{K}(\bar{\sigma} - \bar{\sigma}_0) + \frac{\alpha}{K}(p - p_0)\right] = 1 \tag{30}$$

Consequently, we have

$$\bar{\sigma} - \bar{\sigma}_0 = \alpha(p - p_0) \tag{31}$$

The expressions of global and local strains are modified as

$$\varepsilon_{bs} - \varepsilon_{bs0} = 0 \tag{32}$$

$$\varepsilon_{lfs} - \varepsilon_{lfs0} = -\frac{\varepsilon_{Lm}}{\phi_{or}}\left(\frac{p}{p + p_{Lm}} - \frac{p_0}{p_0 + p_{Lm}}\right)r_{inv}, \quad \text{for } 0 \le t \le \frac{L_{m0}^2}{4\eta_m} \tag{33a}$$

$$\varepsilon_{lfs} - \varepsilon_{lfs0} = -\frac{\varepsilon_{Lm}}{\phi_{or}}\left(\frac{p}{p + p_{Lm}} - \frac{p_0}{p_0 + p_{Lm}}\right), \quad \text{for } t > \frac{L_{m0}^2}{4\eta_m} \tag{33b}$$

Substituting eqs 31−33 into eqs 25a and 25b yields the apparent permeability ratio for constant volume conditions. Input parameters of the constant total volume case are the same as case 3. It can be seen from Figure 12(a) that the permeability would first decline due to the sorption-induced volumetric strain. When the maximum swelling strain is achieved and a new equilibrium state occurs, the permeability becomes stable. As for permeability maps, the upper limit is a horizontal line with a unit permeability ratio, while the lower boundary is, once again, controlled by sorption parameters.

5.3. Nonuniform Matrix-Fracture Systems. In this study, the shale rocks are idealized as a matrix-block and fracture-network interwoven structure with a uniform fracture (pore) distribution. In fact, the actual distribution of matrix blocks and fractures (pores) may not be uniform, and their properties conform to certain characteristics.[34,62,63] The fractal theory can be utilized to characterize the nonuniform distribution of fracture spacing/aperture. As for the permeability evolution curve, the nonuniform distributed properties can affect the duration and shape of the v-shaped (for gas injection) or n-shaped (for gas depletion) matrix-fracture interaction period and the final stable permeability. This is because the evolution of matrix and fracture properties is nonuniform. Therefore, the final evolution result (final permeability) and evolution behavior (the v-shaped or n-shaped section) deviate from the homogeneous ones.

https://dx.doi.org/10.1021/acs.energyfuels.0c00219
Energy Fuels 2020, 34, 4393−4406

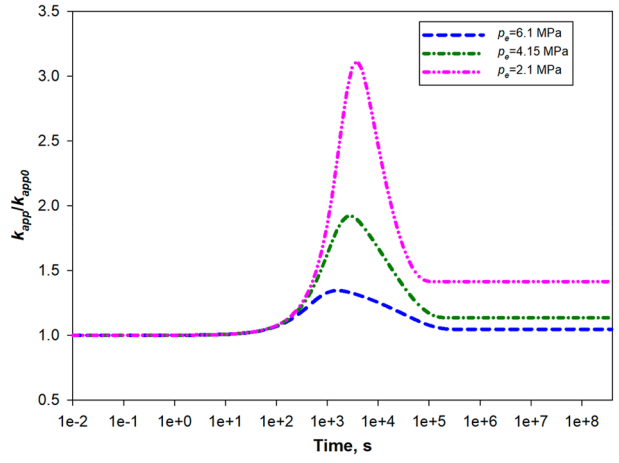

(a)

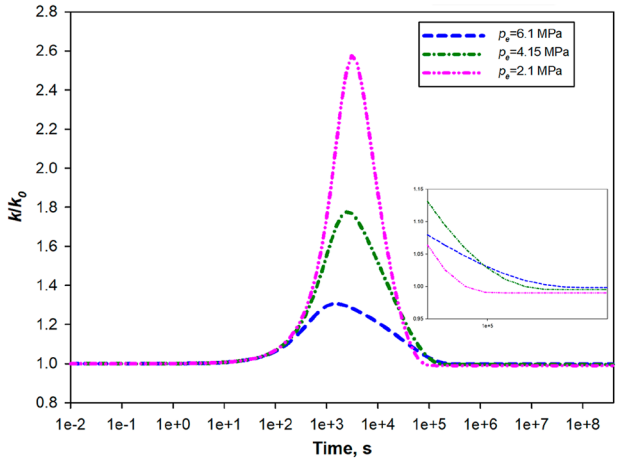

(b)

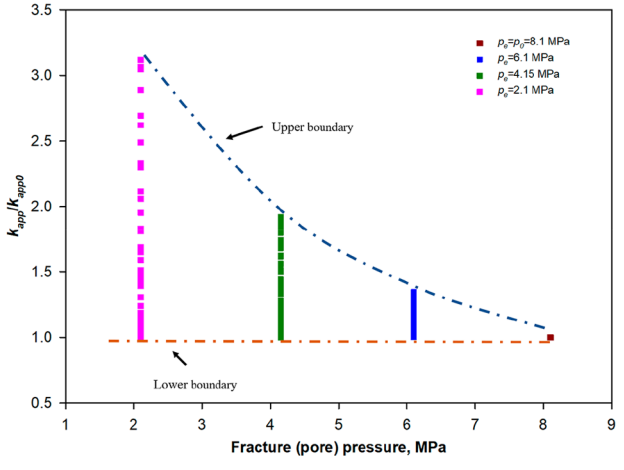

(c)

Figure 9. Shale permeability evolution during gas extraction under a constant Terzaghi effective stress condition: (a) simulation results; (b) simulation results without flow regime's influence; and (c) a shale permeability map.

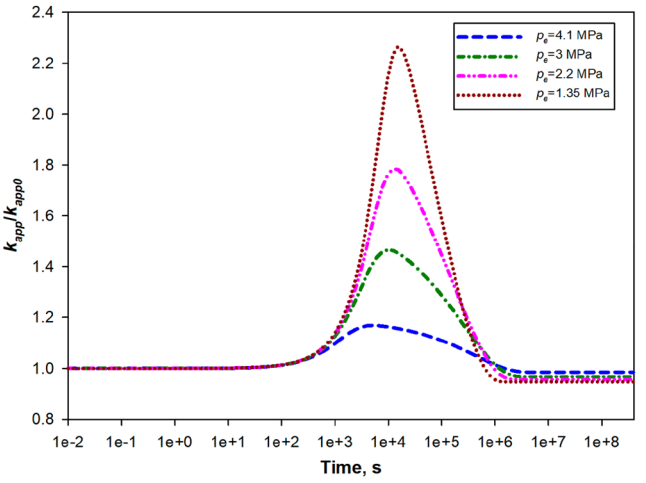

(a)

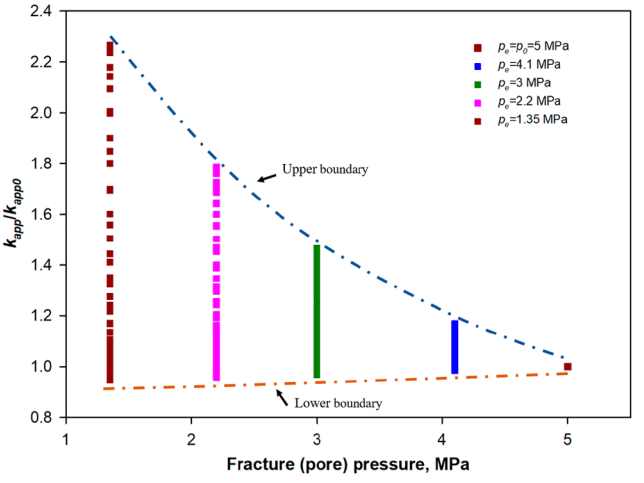

(b)

Figure 10. Shale permeability evolution during gas extraction under a constant confining pressure condition: (a) simulation results and (b) a permeability map.

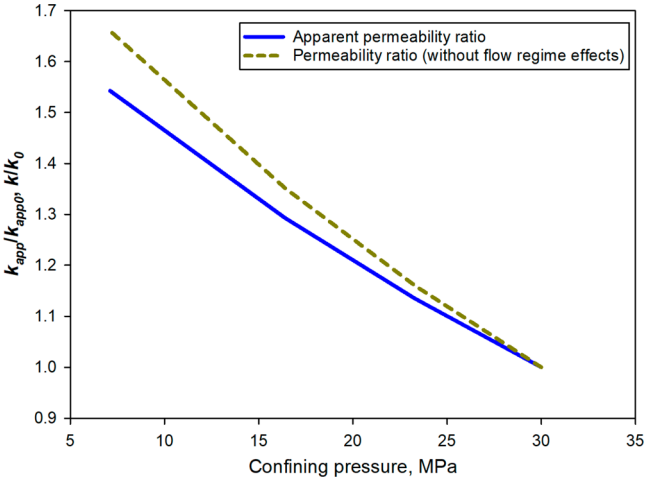

Figure 11. Comparison of simulation results for a constant average fracture (pore) pressure case.

5.4. Applications for Shale Gas Extraction. In this section, we would like to introduce how this model can be applied to shale gas extraction. In order to simulate shale gas production, the permeability and porosity models need to be inserted into a fully coupled gas-transport and shale-deformation system. Our permeability and porosity models

https://dx.doi.org/10.1021/acs.energyfuels.0c00219
Energy Fuels 2020, 34, 4393−4406

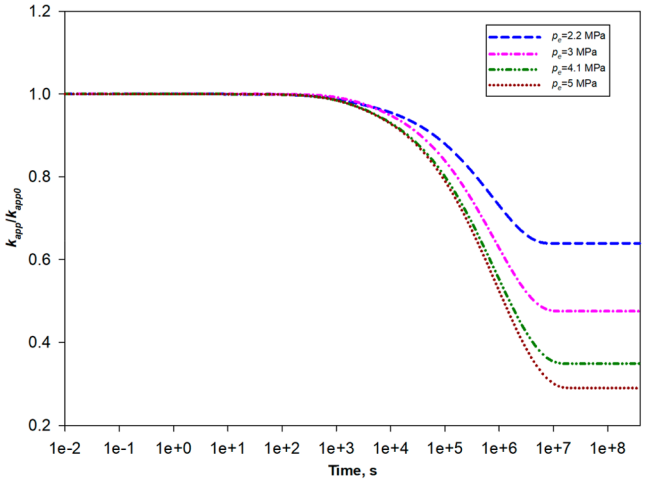

(a)

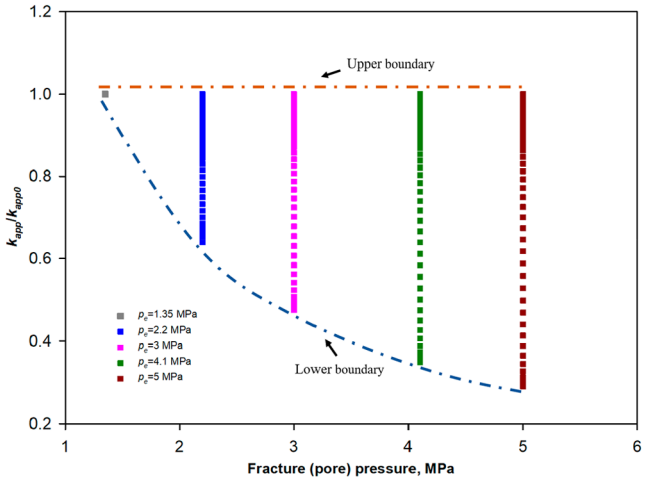

(b)

Figure 12. Shale permeability evolution during gas injection under a constant total volume condition: (a) simulation results and (b) a permeability map.

are basically two piecewise functions. Similar to our previous studies,[11,17,19,36] the permeability and porosity models can be substituted into the following mass balance equation

$$\frac{\partial\left(\rho_g\phi + \rho_{ga}\rho_s\frac{V_L p}{p+p_L}\right)}{\partial t} + \nabla\left[\rho_g\left(-\frac{k_{app}}{\mu}\nabla p\right)\right] = 0 \tag{34}$$

where ρ_g is the gas density (kg/m^3), ρ_{ga} is the gas density under the standard condition (kg/m^3), ρ_s is the shale bulk density (kg/m^3), and V_L is the Langmuir volume constant (m^3/kg). The governing equation for shale deformation is

$$Gu_{i,kk} + \frac{G}{1-2\upsilon}u_{k,ki} - \alpha p_{,i} - K\varepsilon_{s,i} + f_i = 0 \tag{35}$$

where $G = E/[2(1+\nu)]$, f_i is the component of the body force (N/m^3), u_i is the displacement component (m), and a comma followed by subscripts represents differentiation with respect to spatial coordinates and repeated indices in the same monomial depict summation over the range of the indices. The mass balance equation and the governing equation for shale deformation define the coupled gas transport and shale deformation. These equations would be used in and solved by COMSOL Multiphysics, a partial-differential-equation solver. The piecewise functions can be edited by the COMSOL Multiphysics language as input properties. The mean normal stress $\bar{\sigma}$ can be obtained from the boundary loadings, while the fracture (pore) pressure p is automatically obtained by solving the partial differential equations. The depleted matrix area expansion is included. The volume ratio is used to depict local shrinkage, and the diffusivity is defined as the product of intrinsic diffusivity (η_m) and a pressure difference coefficient, $(p - p_0)/(p_{wf} - p_0)$. This coefficient ranges from zero to one, and p_{wf} is the constant wellbore pressure (Pa). Therefore, the depleted matrix area expansion speed depends on the pressure difference. When gas production starts, there is a pressure wave that propagates from the well to the reservoir boundary. Before the pressure wave reaches the undrained formation, there are no pressure differences and no local effects. When the pressure wave approaches a certain area of the formation, the pressure difference of this area would increase later, and the depleted matrix area expansion speed would also increase, resulting in local effects. We use the intrinsic diffusivity in our experiment analyses, because the core size is very small compared with a gas field and can be treated as a bulk rock without considering the pressure wave propagation in the field scale.

6. CONCLUSIONS

A shale permeability map covers the evolution of shale permeability from initial to ultimate equilibrium states. When an equilibrium state is reached, the swelling/shrinkage is normally assumed as uniform within the matrix. Therefore, the shale permeability map also represents the evolution of shale permeability from initial to ultimate uniform swelling/shrinkage within the matrix. On the basis of our modeling results, the following major conclusions can be drawn:

(1) The commonly used matrix-fracture equilibrium assumption of permeability models is only applicable for the initial equilibrium and fully invaded/depleted states. The permeability evolution in between changes significantly as a result of the nonuniform matrix swelling/shrinkage induced by gas diffusion/extraction processes from fracture walls to the inner matrix. The nonuniform matrix deformation ends when matrix rocks are fully invaded/depleted.

(2) During the nonuniform matrix swelling/shrinkage period, permeability curves exhibit time-dependent multistage permeability evolution laws. Localized deformation affects permeability at early times. Then, the dominant factor for permeability evolution shifts from localized deformation to global deformation. The nonuniform deformation (matrix-fracture nonequilibrium) period can be considerably long. The nonequilibrium time scale depends on the level of matrix-fracture property contrast.

(3) The invaded/depleted volume ratio concept provides an effective way to describe nonuniform matrix swelling/depletion strains. Our solutions are consistent with experimental observations. Permeability maps generated based on the nonuniform matrix swelling/shrinkage assumption are capable for explaining permeability data from a broad variety of experimental conditions for both gas injection and depletion. The permeability evolution laws for different testing conditions are quite divergent.

https://dx.doi.org/10.1021/acs.energyfuels.0c00219
Energy Fuels 2020, 34, 4393−4406

AUTHOR INFORMATION

Corresponding Author

Jishan Liu − *School of Engineering, The University of Western Australia, Perth, Western Australia 6009, Australia;* orcid.org/0000-0002-2744-0319; Email: jishan.liu@uwa.edu.au

Authors

Jie Zeng − *School of Engineering, The University of Western Australia, Perth, Western Australia 6009, Australia*

Wai Li − *School of Engineering, The University of Western Australia, Perth, Western Australia 6009, Australia*

Yee-Kwong Leong − *School of Engineering, The University of Western Australia, Perth, Western Australia 6009, Australia*

Derek Elsworth − *Department of Energy and Mineral Engineering, G3 Center and Energy Institute, The Pennsylvania State University, University Park, Pennsylvania 16802, United States*

Jianchun Guo − *State Key Laboratory of Oil and Gas Reservoir Geology and Exploitation, Southwest Petroleum University, Chengdu 610500, China*

Complete contact information is available at: https://pubs.acs.org/10.1021/acs.energyfuels.0c00219

Notes

The authors declare no competing financial interest.

ACKNOWLEDGMENTS

This work is supported by the Australian Research Council under Grant DP200101293, UWA China Scholarships, and the China Scholarship Council (CSC No. 201707970011). Parts of this work have been completed to fulfill the Ph.D. degree requirements of J.Z. at the University of Western Australia.

REFERENCES

(1) Moghadam, A. A.; Chalaturnyk, R. Laboratory investigation of shale permeability. In *SPE/CSUR Unconventional Resources Conference*; Society of Petroleum Engineers: 2015; DOI: 10.2118/175919-MS.

(2) Darcy, H. P. G. *Les Fontaines publiques de la ville de Dijon. Exposition et application des principes à suivre et des formules à employer dans les questions de distribution d'eau, etc.*; Dalamont, V., Ed.; 1856.

(3) Klinkenberg, L. J. The permeability of porous media to liquids and gases. In *Drilling and production practice*; American Petroleum Institute: 1941.

(4) Somerton, W. H.; Söylemezoğlu, I. M.; Dudley, R. C. Effect of stress on permeability of coal. *International journal of rock mechanics and mining sciences & geomechanics abstracts* **1975**, *12* (5−6), 129−145.

(5) Wang, Y.; Meng, F.; Wang, X.; Baud, P.; Wong, T. F. Effective stress law for the permeability and deformation of four porous limestones. *Journal of Geophysical Research: Solid Earth* **2018**, *123* (6), 4707−4729.

(6) Zoback, M. D.; Byerlee, J. D. Permeability and effective stress: Geologic notes. *AAPG Bull.* **1975**, *59* (1), 154−158.

(7) Walsh, J. B. Effect of pore pressure and confining pressure on fracture permeability. *International Journal of Rock Mechanics and Mining Sciences & Geomechanics Abstracts* **1981**, *18* (5), 429−435.

(8) David, C.; Wong, T. F.; Zhu, W.; Zhang, J. Laboratory measurement of compaction-induced permeability change in porous rocks: Implications for the generation and maintenance of pore pressure excess in the crust. *Pure Appl. Geophys.* **1994**, *143* (1−3), 425−456.

(9) Mohiuddin, M.; Korvin, G.; Abdulraheem, A.; Awal, M. R.; Khan, K.; Khan, M. S.; Hassan, H. Stress-dependent porosity and permeability of a suite of samples from Saudi Arabian sandstone and limestone reservoirs. In *International symposium of the society of core analysts*; Abu Dhabi, 2000.

(10) Cui, X.; Bustin, R. M. Volumetric strain associated with methane desorption and its impact on coalbed gas production from deep coal seams. *AAPG Bull.* **2005**, *89* (9), 1181−1202.

(11) Zhang, H.; Liu, J.; Elsworth, D. How sorption-induced matrix deformation affects gas flow in coal seams: a new FE model. *International Journal of Rock Mechanics and Mining Sciences* **2008**, *45* (8), 1226−1236.

(12) Shi, Y.; Wang, C. Y. Pore pressure generation in sedimentary basins: overloading versus aquathermal. *J. Geophys. Res.* **1986**, *91* (B2), 2153−2162.

(13) Gray, I. Reservoir engineering in coal seams: Part 1-The physical process of gas storage and movement in coal seams. *SPE Reservoir Eng.* **1987**, *2* (01), 28−34.

(14) Seidle, J. P.; Jeansonne, M. W.; Erickson, D. J. Application of matchstick geometry to stress dependent permeability in coals. In *SPE Rocky Mountain Regional Meeting*; Society of Petroleum Engineers: 1992; DOI: 10.2118/24361-MS.

(15) Palmer, I.; Mansoori, J. How permeability depends on stress and pore pressure in coalbeds: a new model. In *SPE annual technical conference and exhibition*; Society of Petroleum Engineers: 1996; DOI: 10.2118/36737-MS.

(16) Shi, J. Q.; Durucan, S. Drawdown induced changes in permeability of coalbeds: a new interpretation of the reservoir response to primary recovery. *Transp. Porous Media* **2004**, *56* (1), 1−16.

(17) Cao, P.; Liu, J.; Leong, Y. K. General gas permeability model for porous media: bridging the gaps between conventional and unconventional natural gas reservoirs. *Energy Fuels* **2016**, *30* (7), 5492−5505.

(18) Liu, H. H.; Rutqvist, J. A new coal-permeability model: internal swelling stress and fracture-matrix interaction. *Transp. Porous Media* **2010**, *82* (1), 157−171.

(19) Peng, Y.; Liu, J.; Pan, Z.; Connell, L. D.; Chen, Z.; Qu, H. Impact of coal matrix strains on the evolution of permeability. *Fuel* **2017**, *189*, 270−283.

(20) Peng, Y.; Liu, J.; Wei, M.; Pan, Z.; Connell, L. D. Why coal permeability changes under free swellings: New insights. *Int. J. Coal Geol.* **2014**, *133*, 35−46.

(21) Zhang, S.; Liu, J.; Wei, M.; Elsworth, D. Coal permeability maps under the influence of multiple coupled processes. *Int. J. Coal Geol.* **2018**, *187*, 71−82.

(22) Shi, R.; Liu, J.; Wei, M.; Elsworth, D.; Wang, X. Mechanistic analysis of coal permeability evolution data under stress-controlled conditions. *International Journal of Rock Mechanics and Mining Sciences* **2018**, *110*, 36−47.

(23) Ma, X.; Li, X.; Zhang, S.; Zhang, Y.; Hao, X.; Liu, J. Impact of local effects on the evolution of unconventional rock permeability. *Energies* **2019**, *12* (3), 478.

(24) Liu, X.; Sheng, J.; Liu, J.; Hu, Y. Evolution of coal permeability during gas injection—From initial to ultimate equilibrium. *Energies* **2018**, *11* (10), 2800.

(25) Ferrell, H. H.; Felsenthal, M. Effect of overburden pressure on flow capacity in a deep oil reservoir. *JPT, J. Pet. Technol.* **1962**, *14* (09), 962−966.

(26) Thomas, R. D.; Ward, D. C. Effect of overburden pressure and water saturation on gas permeability of tight sandstone cores. *JPT, J. Pet. Technol.* **1972**, *24* (02), 120−124.

(27) Wang, J. A.; Park, H. D. Fluid permeability of sedimentary rocks in a complete stress-strain process. *Eng. Geol.* **2002**, *63* (3−4), 291−300.

(28) Heller, R.; Vermylen, J.; Zoback, M. Experimental investigation of matrix permeability of gas shales. *AAPG Bull.* **2014**, *98* (5), 975−995.

(29) Yang, D.; Wang, W.; Chen, W.; Wang, S.; Wang, X. Experimental investigation on the coupled effect of effective stress and gas slippage on the permeability of shale. *Sci. Rep.* **2017**, *7*, 44696.

(30) Wei, M.; Liu, J.; Shi, R.; Elsworth, D.; Liu, Z. Long-term evolution of coal permeability under effective stresses gap between matrix and fracture during CO 2 injection. *Transp. Porous Media* **2019**, *130* (3), 969−983.

(31) Jin, G.; Pérez, H. G.; Agrawal, G.; Khodja, M. R.; Ali, A. Z.; Hussaini, S. R.; Jangda, Z. Z. The impact of gas adsorption and composition on unconventional shale permeability measurement. In *SPE Middle east oil & gas show and conference*; Society of Petroleum Engineers: 2015; DOI: 10.2118/172744-MS.
(32) Pini, R.; Ottiger, S.; Burlini, L.; Storti, G.; Mazzotti, M. Role of adsorption and swelling on the dynamics of gas injection in coal. *J. Geophys. Res.* **2009**, DOI: 10.1029/2008JB005961.
(33) Robertson, E. P.; Christiansen, R. L. Modeling permeability in coal using sorption-induced strain data. In *SPE Annual Technical Conference and Exhibition*; Society of Petroleum Engineers: 2005; DOI: 10.2118/97068-MS.
(34) Sheng, G.; Zhao, H.; Su, Y.; Javadpour, F.; Wang, C.; Zhou, Y.; Liu, J.; Wang, H. An analytical model to couple gas storage and transport capacity in organic matter with noncircular pores. *Fuel* **2020**, *268*, 117288.
(35) Sun, Z.; Shi, J.; Wu, K.; Zhang, T.; Feng, D.; Huang, L.; Shi, Y.; Ramachandran, H.; Li, X. An analytical model for gas transport through elliptical nanopores. *Chem. Eng. Sci.* **2019**, *199*, 199−209.
(36) Peng, Y.; Liu, J.; Pan, Z.; Qu, H.; Connell, L. Evolution of shale apparent permeability under variable boundary conditions. *Fuel* **2018**, *215*, 46−56.
(37) Pan, Z.; Connell, L. D. Modelling permeability for coal reservoirs: a review of analytical models and testing data. *Int. J. Coal Geol.* **2012**, *92*, 1−44.
(38) van Golf-Racht, T. D. *Fundamentals of fractured reservoir engineering*; Elsevier: 1982; Vol. *12*.
(39) Reiss, L. H. *The reservoir engineering aspects of fractured formations*; Editions Technip: 1980; Vol. 3.
(40) Beskok, A.; Karniadakis, G. E. Report: a model for flows in channels, pipes, and ducts at micro and nano scales. *Microscale Thermophys. Eng.* **1999**, *3* (1), 43−77.
(41) Karniadakis, G.; Beskok, A.; Aluru, N. *Microflows and nanoflows: fundamentals and simulation*; Springer Science & Business Media: 2006; Vol. *29*, DOI: 10.1007/0-387-28676-4.
(42) Javadpour, F.; Fisher, D.; Unsworth, M. Nanoscale gas flow in shale gas sediments. *Journal of Canadian Petroleum Technology* **2007**, *46* (10), 55−61.
(43) Moghadam, A. A.; Chalaturnyk, R. Analytical and experimental investigations of gas-flow regimes in shales considering the influence of mean effective stress. *SPE Journal* **2016**, *21* (02), 557−572.
(44) Wu, K.; Chen, Z.; Li, X. Real gas transport through nanopores of varying cross-section type and shape in shale gas reservoirs. *Chem. Eng. J.* **2015**, *281*, 813−825.
(45) White, F. M.; Corfield, I. *Viscous fluid flow*; McGraw-Hill: New York, 2006; Vol. 3, pp 433−434.
(46) Cao, P.; Liu, J.; Leong, Y. K. Combined impact of flow regimes and effective stress on the evolution of shale apparent permeability. *Journal of Unconventional Oil and Gas Resources* **2016**, *14*, 32−43.
(47) Dong, J.; Cheng, Y.; Liu, Q.; Zhang, H.; Zhang, K.; Hu, B. Apparent and true diffusion coefficients of methane in coal and their relationships with methane desorption capacity. *Energy Fuels* **2017**, *31* (3), 2643−2651.
(48) Civan, F.; Rai, C. S.; Sondergeld, C. H. Determining shale permeability to gas by simultaneous analysis of various pressure tests. *SPE Journal* **2012**, *17* (03), 717−726.
(49) Peng, Y.; Liu, J.; Pan, Z.; Connell, L. D. A sequential model of shale gas transport under the influence of fully coupled multiple processes. *J. Nat. Gas Sci. Eng.* **2015**, *27*, 808−821.
(50) Liu, J.; Wang, J.; Chen, Z.; Wang, S.; Elsworth, D.; Jiang, Y. Impact of transition from local swelling to macro swelling on the evolution of coal permeability. *Int. J. Coal Geol.* **2011**, *88* (1), 31−40.
(51) Cui, G.; Liu, J.; Wei, M.; Shi, R.; Elsworth, D. Why shale permeability changes under variable effective stresses: new insights. *Fuel* **2018**, *213*, 55−71.
(52) Josh, M.; Esteban, L.; Delle Piane, C.; Sarout, J.; Dewhurst, D. N.; Clennell, M. B. Laboratory characterisation of shale properties. *J. Pet. Sci. Eng.* **2012**, *88*, 107−124.
(53) Rybacki, E.; Reinicke, A.; Meier, T.; Makasi, M.; Dresen, G. What controls the mechanical properties of shale rocks?-Part I: Strength and Young's modulus. *J. Pet. Sci. Eng.* **2015**, *135*, 702−722.
(54) Yuan, W.; Li, X.; Pan, Z.; Connell, L. D.; Li, S.; He, J. Experimental investigation of interactions between water and a lower Silurian Chinese shale. *Energy Fuels* **2014**, *28* (8), 4925−4933.
(55) Lyu, Q.; Long, X.; Ranjith, P. G.; Tan, J.; Kang, Y.; Wang, Z. Experimental investigation on the mechanical properties of a low-clay shale with different adsorption times in sub-/super-critical CO2. *Energy* **2018**, *147*, 1288−1298.
(56) Islam, M. A.; Skalle, P. An experimental investigation of shale mechanical properties through drained and undrained test mechanisms. *Rock Mechanics and Rock Engineering* **2013**, *46* (6), 1391−1413.
(57) Ziarani, A. S.; Aguilera, R. Knudsen's permeability correction for tight porous media. *Transp. Porous Media* **2012**, *91* (1), 239−260.
(58) Guo, F. *Experimental Methods of Shale Permeability*, Master's thesis, The University of Western Australia, Perth, 2014.
(59) Kumar, H.; Elsworth, D.; Mathews, J. P.; Marone, C. Permeability evolution in sorbing media: analogies between organic-rich shale and coal. *Geofluids* **2016**, *16* (1), 43−55.
(60) Sone, H.; Zoback, M. D. Mechanical properties of shale-gas reservoir rocks—Part 1: Static and dynamic elastic properties and anisotropy. *Geophysics* **2013**, *78* (5), D381−D392.
(61) Ghanizadeh, A.; Amann-Hildenbrand, A.; Gasparik, M.; Gensterblum, Y.; Krooss, B. M.; Littke, R. Experimental study of fluid transport processes in the matrix system of the European organic-rich shales: II. Posidonia Shale (Lower Toarcian, northern Germany). *Int. J. Coal Geol.* **2014**, *123*, 20−33.
(62) Montazeri, G. H.; Tahami, S. A.; Moradi, B.; Safari, E. Effects of different block size distributions in pressure transient response of naturally fractured reservoirs. *Brazilian Journal of Petroleum and Gas* **2011**, *5* (3), 139−147.
(63) Zeng, J.; Li, W.; Liu, J.; Leong, Y. K.; Elsworth, D.; Tian, J.; Guo, J.; Zeng, F. Analytical solutions for multi-stage fractured shale gas reservoirs with damaged fractures and stimulated reservoir volumes. *J. Pet. Sci. Eng.* **2020**, *187*, 106686.

https://dx.doi.org/10.1021/acs.energyfuels.0c00219
Energy Fuels 2020, 34, 4393−4406